

Experimental observation of hydrodynamic-like behavior in 3D topological semimetal ZrTe₅

Chang-woo Cho (✉ chang-woo.cho@lncmi.cnrs.fr)

Grenoble high magnetic field laboratory <https://orcid.org/0000-0002-5190-7070>

Peipei Wang

Department of Physics, Southern University of Science and Technology of China

Fangdong Tang

Southern University of Science and Technology

Sungkyun Park

Pusan National University <https://orcid.org/0000-0003-1816-310X>

Mingquan He

College of Physics, Chongqing University

Rolf Lortz

Hong Kong University of Science and Technology

Genda Gu

Brookhaven National Laboratory

Liyuan Zhang

Southern University of Science and Technology <https://orcid.org/0000-0001-7968-3294>

Article

Keywords: hydrodynamic fluidity, condensed matter physics, Wiedemann-Franz law

Posted Date: January 22nd, 2021

DOI: <https://doi.org/10.21203/rs.3.rs-148697/v1>

License:  This work is licensed under a Creative Commons Attribution 4.0 International License.

[Read Full License](#)

Experimental observation of hydrodynamic-like behavior in 3D topological semimetal ZrTe₅

Chang-woo Cho^{1,2}, Peipei Wang¹, Fangdong Tang¹, Sungkyun Park²,
Mingquan He³, Rolf Lortz⁴, Genda Gu⁵, and Liyuan Zhang^{1,+}

¹*Department of Physics, Southern University of Science and Technology, Shenzhen 518055,
China*

²*Department of Physics, Pusan National University, Busan 46241, South Korea*

³*Low Temperature Physics Lab, College of Physics & Center of Quantum Materials and
Devices, Chongqing University, Chongqing 401331, China*

⁴*Department of Physics, The Hong Kong University of Science and Technology, Clear Water
Bay, Kowloon, Hong Kong*

⁵*Condensed Matter Physics and Materials Science Department, Brookhaven National
Laboratory, Upton, NY 11973, USA*

Hydrodynamic fluidity in condensed matter physics has been experimentally demonstrated only in a limited number of compounds because of the stringent conditions that must be satisfied. Herein, we demonstrate the existence of hydrodynamic-like properties driven by the collective excitation of the Dirac fluid in the three-dimensional topological semimetal ZrTe₅. By measuring the electrical and thermal properties in a wide temperature range, we find a regime satisfying phononic hydrodynamic-like characteristics with two representative experimental evidences: a faster evolution of the thermal conductivity than in the ballistic regime and the existence of a local maximum of the effective mean free path. In contrast to phononic hydrodynamics, the Wiedemann-Franz law is violated by about a factor of 100. Moreover, phonon-dragged anomalies are observed, which serve as a signature of the Dirac fluidity in this system.

⁺ corresponding author: zhangly@sustech.edu.cn

Introduction

Phonon-dominant heat conduction is described by Fourier's law, in which phonons scatter from other phonons, impurities, and interfaces¹⁻³. This process takes place through the momentum-relaxing process known as Umklapp scattering (hereafter U-scattering). During this process, heat currents are dissipated and the crystal momentum is not conserved¹⁻³. On the other hand, Fourier's law is no longer valid when the temperature T is sufficiently low in which the crystal momentum is conserved due to dominant Normal scattering (hereafter N-scattering)⁴⁻⁶. These two types of scattering mechanisms are known for a diffusive and a ballistic regime, respectively, and have been confirmed in many materials for over 50 years⁴⁻⁶.

Meanwhile, unusual transport phenomena between the ballistic and the diffusive regimes have recently been reported on low-dimensional materials⁷⁻¹², in which thermal conductivity κ evolves more rapidly than in the ballistic regime^{8,12}. Such an intermediate region is called hydrodynamic because it is analogous to macroscopic transport phenomena in water fluids^{13,14}. Two different characteristics are known in the phonon hydrodynamic system: the Poiseuille flow and the second-sound¹⁴⁻¹⁶. The former is characterized by a steady-state phonon flow where thermal resistance diffuses due to the boundary scattering combined with N-scattering. In comparison, the latter is the wave-propagation of a T gradient without significant attenuation. The phonon Poiseuille flow could be confirmed by the T and sample width dependencies of κ ^{8,9,12}.

Despite the fascination of hydrodynamics in solid state systems, it has been observed only in a narrow T range and required remarkably low- T with abundant N-scattering as well as a suitable sample size. For example, the reported T range for phonon Poiseuille flow is 0.5 – 1.0 K in suspended graphene^{7,16}. This is because U-scattering overwhelms N-scattering in almost every T range except for significantly low temperatures. In this T range, electrons rather than phonons are the primary heat carriers. For these reasons, phonon-hydrodynamic behavior has been experimentally demonstrated in less than a handful of compounds, such as black P⁹, SrTiO₃¹⁷, and thin-graphite⁸. Therefore, the search for new materials in which hydrodynamics contributed by phonons or other collective excitations can be observed is of great interest to the condensed matter community.

In this study, we performed thermal and electrical transport experiments for ZrTe₅ single crystals to investigate the hydrodynamic property. In fact, the ZrTe₅ study is initiated decades ago due to its considerable thermoelectric performance and its resistivity anomaly. Recently, it has gained renewed attention due to non-trivial topological phenomena such as a 3D quantum Hall effect¹⁸, a quantum spin Hall effect on a monolayer¹⁹, and a chiral magnetic effect²⁰. Moreover, bulk ZrTe₅ has been reported to sit at the boundary between a weak- and strong-topological insulator so that external perturbation easily influences its topology²¹⁻²³. Herein, Dirac-Fluid (DF) hydrodynamics could be added to a new list of exotic physical properties in ZrTe₅. We present two experimental signatures for phonon hydrodynamics: a faster κ

evolution than in the ballistic regime and a local maximum of the effective mean-free-path (MFP). In contrast to conventional phonon hydrodynamics, we additionally observe the phonon-dragged anomalies near the onset of a hydrodynamic regime with an exceptionally strongly violated Lorentz ratio. These observations have important implications for ongoing research on the various possible types of quasiparticle hydrodynamics, especially in a three-dimensional topological semimetal material.

Results

Since our primary interest is the hydrodynamic-like system, it is essential to verify that the samples used in this study are clean enough. Otherwise, it is hard to observe even at low T due to the lack of N-scattering. **Figure 1a** presents the electrical resistivity in a temperature range from 0.3 to 300 K at zero magnetic field. A characteristic peak around ~ 90 K (T_p) is seen in both samples (Sample #1: 84 K and Sample #2: 89 K), indicating that the Fermi level moves from valence band to conduction band as T decreases²⁴. In **Fig. 1b** and **c**, we depict the T -dependent dominant charge carrier density n and mobility μ , respectively. Both quantities are extracted from a two-band model fit ($T > 40$ K) and the linear fit near the zero-field data of the Hall measurement ($T < 40$ K). There is an obvious sign change of n with the exceptionally low density ($\sim 10^{16}$ to $\sim 10^{17}$ cm⁻³) and the gradual increase of μ with ultrahigh values ($\sim 10^5$ to $\sim 10^6$ cm²V⁻¹s⁻¹) at low T . All values are comparable to our previous observation¹⁸, which guarantees the excellent crystalline quality of the samples and allows us to examine a hydrodynamic-like regime.

In the following, let us examine the transport evidence for the hydrodynamics in our ZrTe₅. The first clue is to find a κ that evolves faster than T^3 . To test this, we plot the T dependence of the total thermal conductivity κ_{tot} (open squares in Sample #1 and circles in Sample #2), and the electronic thermal conductivity κ_e (solid lines) in **Fig. 2**. Note that only κ_{tot} is a directly measured value, while κ_e is derived from the Wiedemann-Franz (WF) law ($\kappa_e = \frac{T}{\rho} L_0$, Lorenz number $L_0 = 2.44 \times 10^{-8}$ W Ω K⁻²). For clarity, it is plotted on a log-log scale here. In the high T regime (between about 30 K to 300 K), it is governed by the perfect $1/T$ dependence in all the samples (see supplementary **Fig. S2**), implying that the U-scattering is the most prominent process in this range. After passing through the κ_{tot} maximum, it starts to decrease, indicating the N-scattering process begins to dominate. For Sample #2, the slope of κ_{tot} gradually increases towards low T and exceeds a T^5 dependence below ~ 2 K (dashed line in **Fig. 2**). Sample #1 behaves similarly with a slightly slower increase in slope. It should be mentioned that κ_e shows an irregular behavior at sufficiently low T , where it must converge to κ_{tot} , since the thermal energy at low T is mainly transferred from the charge carriers. However, we see no convergence up to the experimental low T -limit. Below 1 K, κ_e is still

smaller than κ_{tot} by a factor of a few 100. We will discuss more details later in the context of the large-violation of the WF-law.

Near the hydrodynamic-like regime, we find additional anomalies. In **Fig. 3a** and **b**, we present the enlarged curves of the electrical resistivity ρ and κ_{tot} versus T for Sample #2. At first glance, ρ exhibits a typical T^2 Fermi-liquid (*FL*) behavior in the 6 - 30 K range. Upon further cooling, ρ begins to deviate from the *FL* behavior below ~ 6 K (T_a), with a pronounced downward curvature, but remaining at a finite value. A power-law scaling (i.e., $\rho = \rho_0 + AT^2$) between 6 and 30 K yields a residual resistivity $\rho_0 \approx 0.154 \text{ m}\Omega \text{ cm}$ and the pre-factor $A \approx 0.098 \text{ m}\Omega \text{ cm K}^{-2}$. In the κ_{tot} versus T data (**Fig. 3b**), a step-like anomaly occurs at a temperature that is in perfect agreement with T_a . The origin of the breakdown of *FL* behavior as well as a κ anomaly maybe naively interpreted as originating from traces of superconductivity in the sample. However, a comparison with Ref ²⁵, in which a hydrostatic pressure as high as 6.7 GPa was required to induce superconductivity with a sharp $T_c \sim 1.8$ K, makes the presence of superconducting correlations at ambient pressure quite unlikely. Moreover, they estimated the upper critical field to be about 1.5 T at 14.6 GPa ²⁵, whereas the ρ anomaly observed in our ZrTe₅ sample is quite robust for much higher applied magnetic fields (see supplementary **Fig. S3**). In fact, such non-*FL* behavior is only seen in Sample #2 as shown in **Fig. 3a** and is likely triggered by slight differences in initial crystal growth conditions. ZrTe₅ is a highly sensitive material to growth conditions and slight differences may somewhat alter its electronic and thermal properties ^{18,22,26}.

On the other hand, a common anomaly for our samples is found in the T -dependent κ/T^3 and Lorenz ratio (L/L_0), as shown in **Fig. 3c** and **d**. These anomalies occur near the onset of a hydrodynamic-like regime. It is reasonable to conclude that such a peaked anomaly could originate from the phonon-drag effect since no sign is seen in the κ_{WF} vs T data (solid lines in **Fig. 2**), representing the purely electronic κ contribution. In Ref ²⁷, a pronounced phonon-drag peak in the low T thermopower was also reported in the Dirac semimetal PtSn₄, where the peak was observed exclusively in the thermal transport data, similar to the present study.

Next, we turn to the effective quasiparticle MFP, another critical signature of phonon hydrodynamics. In most previous studies, the magnitude of the MFP has been estimated by the simple relation $\kappa_{ph} = \frac{1}{3}C_{ph}v_sl_{ph}$, where C_{ph} , v_s , and l_{ph} denote the phonon specific heat, sound velocity, and phonon MFP, respectively ¹⁷. Instead of taking a conventional route, we attempt to measure the thermal Hall effect, as this could be a direct probe to study quasiparticle dynamics, but it has rarely been performed in topological materials due to the difficulty of obtaining high-quality data.

Figure 4a shows the field dependence of the thermal Hall resistivity ω_{xy} ($= \frac{wt}{l} \left(\frac{\Delta T_{xy}}{P} \right)$, where ΔT_{xy} and P denote the T gradient between two points along the transverse direction and the thermopower, respectively) in a narrow B -field range from -1.0 to 1.0 T. In the main text,

only the case of Sample #1 is presented. The value of ω_{xy} is close to zero regardless of the measured temperatures. However, in a weak field region ($|B| < 0.1$ T), an asymmetric thermal Hall feature is found, which becomes stronger as T decreases.

To evaluate the degree of heat deviation, the thermal Hall angle $\tan \theta_H (= \frac{\kappa_{xy}}{\kappa_{xx}})$ is plotted as a function of B -fields at various temperatures (**Fig. 4b**). The trend is not different from ω_{xy} vs B . It shows a significant deviation when B-fields are applied and is abruptly suppressed and eventually disappears in the region of higher B-fields. In **Fig. 4c**, we reveal the zero-field-limit ($B \rightarrow 0$) of $\tan \theta_H / B$ (hereafter $[\tan \theta_H / B]_0$), which is usually proportional to the effective MFP of the quasiparticles²⁸. The magnitude of MFP can be estimated through the equation $l = \frac{\hbar k_F \tan \theta_H}{e B}$, where l is the MFP of quasiparticle, \hbar is the planck constant, k_F is the Fermi wave number, and e is the electron charge²⁹. With the estimation value of $k_F \approx 4 \times 10^{-3} \text{ \AA}^{-1}$ in the ac -plane¹⁸, we obtain the MFP is about 40 μm at 1.0 K, which is comparably longer than the previous results³⁰⁻³². A striking feature of $[\tan \theta_H / B]_0$ is the presence of a local peak (as marked by vertical arrows) corresponding to temperatures at ~ 2 K (Sample #1) and ~ 6 K (Sample #2). These agree well with the onset of the hydrodynamic-like regime we have seen. It is worth noting that the thermal Hall signal is principally from the electronic contribution since the neutrally charged quasiparticles are not affected by a magnetic field. Therefore, the hydrodynamic behavior in our ZrTe_5 samples is attributed to charged quasiparticles.

Discussion

So far, we have shown the hydrodynamic-like features with the electrical and thermal transport results. The following question is what quasiparticle excitations or their interactions cause the hydrodynamics in ZrTe_5 . First of all, we can test the electron-electron hydrodynamic scenario. According to the result of the zero-field-limit electronic Hall-angle ($[\tan \theta_e / B]_0$, see inset of **Fig. 4c**), it continuously increases when T decreases to ~ 10 K and then saturates at low T . This means that the electron-electron scattering process below 10 K is practically unaffected by the entire scattering system.

The next possibility is an electron-phonon fluid in which the electron-phonon scattering process is the fastest so that their momentum can be quasi-conserved. For electron-phonon cases studied previously, the results were similar to ours. For instance, we find the phonon-drag effect in thermal transport and the breakdown of the WF law proposed in Ref²⁷ as evidence for an electron-phonon fluid. One difference with the present study is the magnitude of L/L_0 . Whereas L/L_0 in our ZrTe_5 deviates from 1 over an entire temperature range and has a large value over a few 100 (see **Fig. 3d**), the data presented in PtSn_4 showed a small value of L/L_0

($L/L_0 < 1$) in a hydrodynamic regime. It has been argued that this is indicative of significant inelastic electron-phonon scattering¹¹. In this context, we also rule out the scenario that the electron-phonon interaction induces hydrodynamics in ZrTe₅.

DF is our last choice. This type of strange metal was introduced by Crossno et al to describe the hydrodynamic behavior at the charge neutrality point¹¹. As mentioned earlier, the ZrTe₅ single crystals used exhibit ultra-high mobility due to their exceptionally high-purity, and their bipolar charge carrier types are more or less compensated at low T . These prerequisites for the realization of the DF scenario are perfectly met¹¹. Moreover, the DF is expected to show an enhancement of κ and the largely violated WF law on the order of hundreds of L/L_0 , due to the depairing of charge and heat currents in the hydrodynamic regimes, which is in good agreement with our observations. Finally, the T -dependent Dirac-particle thermal conductivity κ_{DF} also supports this argument. Since the purely phononic thermal conductivity κ_{ph} is less-sensitive to the magnetic field and the electronic contribution is extremely small in our case, as shown in **Fig. 5(a)**, we can extract the approximation of κ_{DF} from $\kappa_{tot}(0\text{ T})$ by subtracting the magneto-thermal conductivity at a sufficiently high B -field. If we then define $\Delta\kappa = \kappa_{tot}(0\text{T}) - \kappa_{tot}(B \neq 0\text{T})$, it is proportional to κ_{DF} , which is presented in **Fig. 5(b)**. When compared with κ_{WF} , the $\Delta\kappa$ is enormously different in the hydrodynamic regime. This is in perfect agreement with the experimental observation of Crossno et al¹¹.

Summary

In summary, the main effort of hydrodynamic studies to date has been to find the significant features where either electrons or phonons provide the primary scattering. However, all transport regimes – ballistic, hydrodynamic and diffusive – can coexist and be coupled, making it more complicated and difficult to differentiate purely quasiparticle hydrodynamic phenomena. Using ultrahigh-purity single crystals of ZrTe₅, we find the transport signature of the hydrodynamic-like behavior, which we attribute to Dirac-quasiparticle excitations. With a significantly violated Lorenz ratio by more than a factor of 100 and a non-trivial transport behavior near the hydrodynamic regime, all our experimental observations point to the DF induced by the charge-neutral plasma of quasi-relativistic fermions.

Acknowledgement

We thank Benjamin Piot and Kitinan Pongsangangan for their enlightening discussions. M. He acknowledges the support by National Natural Science Foundation of China (11904040), Chongqing Research Program of Basic Research and Frontier Technology, China (Grant No.

cstc2020jcyj-msxmX0263), Fundamental Research Funds for the Central Universities, China(2020CDJQY-A056, 2020CDJ-LHZZ-010, 2020CDJQY-Z006), Projects of President Foundation of Chongqing University, China(2019CDXZWL002).

Author contribution

This work was initiated by L.Z.; C.w.C. carried out the electrical and thermal transport measurements with help of P.W., F.T., M.H. and R.L.; the single crystal samples were provided by G.G.; C.w.C. and L.Z. analyzed the data with the help of S.P., M.H. and R.L.; the manuscript was prepared by C.w.C. and L.Z. with the help of S.P. and R.L., and all authors were involved in discussions and contributed to the manuscript.

Competing financial interests

The authors declare no competing financial interests.

Data availability

The data that support the findings of this study are available from the corresponding author upon reasonable request.

Methods

Sample Preparation

Ultra-high quality single crystals of ZrTe_5 were grown by the tellurium flux method. Thanks to the relatively large size of the single acicular crystals ($l \times w \times t$, Sample #1: $3.20 \times 0.30 \times 0.08 \text{ mm}^3$, Sample #2: $2.90 \times 0.30 \times 0.21 \text{ mm}^3$), we were able to perform the electrical and thermal transport experiments on the same bulk samples. Details of the sample growth and structural properties can be found elsewhere ^{18,20,33}. In the main text, we defined the longest (shortest) dimension is along the a -axis (b -axis), corresponding to the stacking layer direction.

Experimental techniques

For the electrical transport measurement, we performed it by the standard Hall bar method, using an alternating current with an amplitude of 0.01-0.1 mA amplitude and a frequency of 10-20 Hz. The magnetic field was applied in the perpendicular direction to the ac -plane. To measure the thermal transport of such an acicular ZrTe_5 crystal, we used a well-known steady-state method with one-heater and three-thermometers. One end of a ~ 4.0 mm long sample was attached to a copper heat sink, while a small ~ 100 Ohm resistor and three well-calibrated Cernox thermometers were connected with Ag (100 μm) and Pt/W wires (25 μm), respectively (see supplementary **Fig. S1**). Using three lock-in amplifiers and three thermometer chips, we were able to obtain the longitudinal and transverse thermal gradients simultaneously. To eliminate spurious longitudinal (or transverse) components, we measured the magneto-thermal conductivity with opposite field directions and averaged them. Since the sensitivity of the thermometers used in this experiment becomes insensitive towards higher temperatures, we switched to a thermocouple method to record the thermal gradient in the high T regime ($T > \sim 20$ K). In the overlapping range (about 10-20 K), we confirmed the consistent κ results within the error bar; an example for Sample #2 is presented in Supplementary **Fig. S2**.

Figures

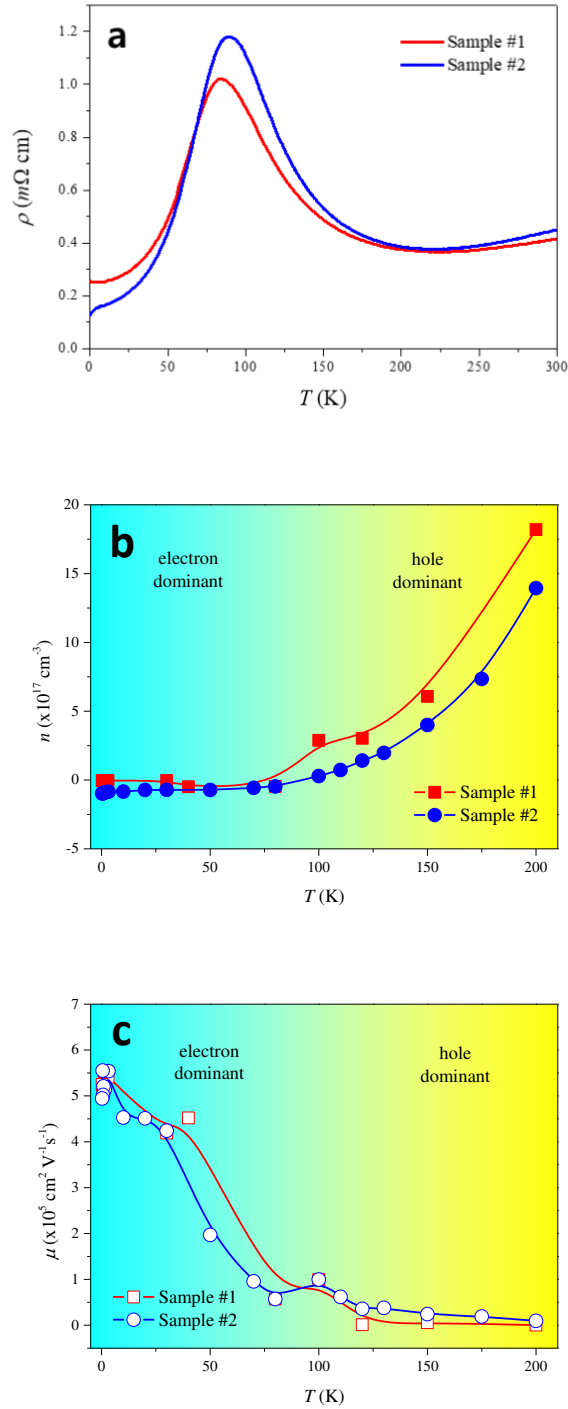


Figure 1. T -dependent electrical resistivity ρ (a), the dominant carrier density n (b), and their mobility μ (c) of ZrTe₅ single crystals. To extract the n and μ , a two-band model was used for high T data (above 40 K), while the values at low T (below 40 K) were taken from the Hall measurement by the linear fitting method.

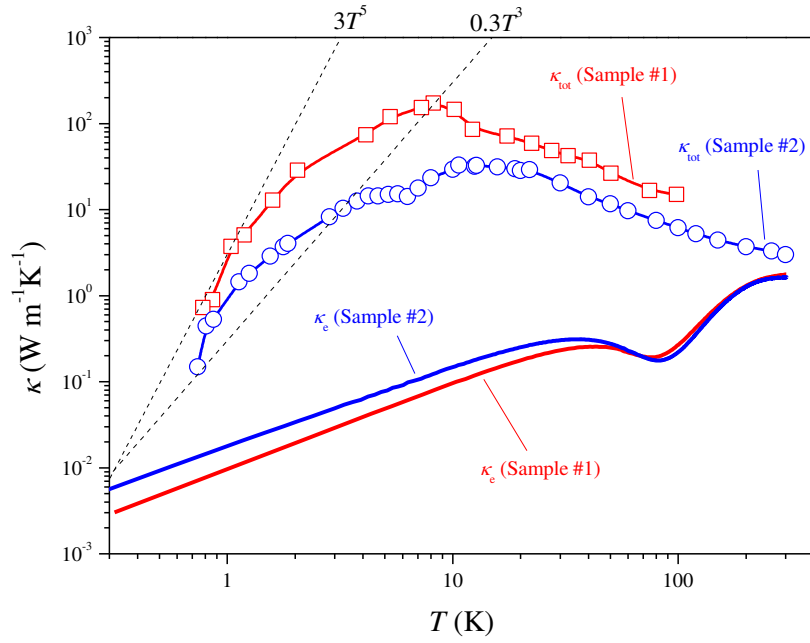


Figure 2. Thermal conductivity as a function of T in a log-log plot for two different ZrTe_5 samples. The open squares (Sample #1) and circles (Sample #2) represent the total thermal conductivity κ_{tot} , and the solid lines denote the charge carrier thermal conductivity κ_e , which is calculated according to the Wiedemann-Franz law ($\kappa_e = \frac{T}{\rho} L_0$, where the Lorenz number $L_0 = 2.44 \times 10^{-8} \text{ W}\Omega\text{K}^{-2}$). The two dashed lines proportional to T^3 and T^5 are added for comparison with the T evolution of κ_{tot} .

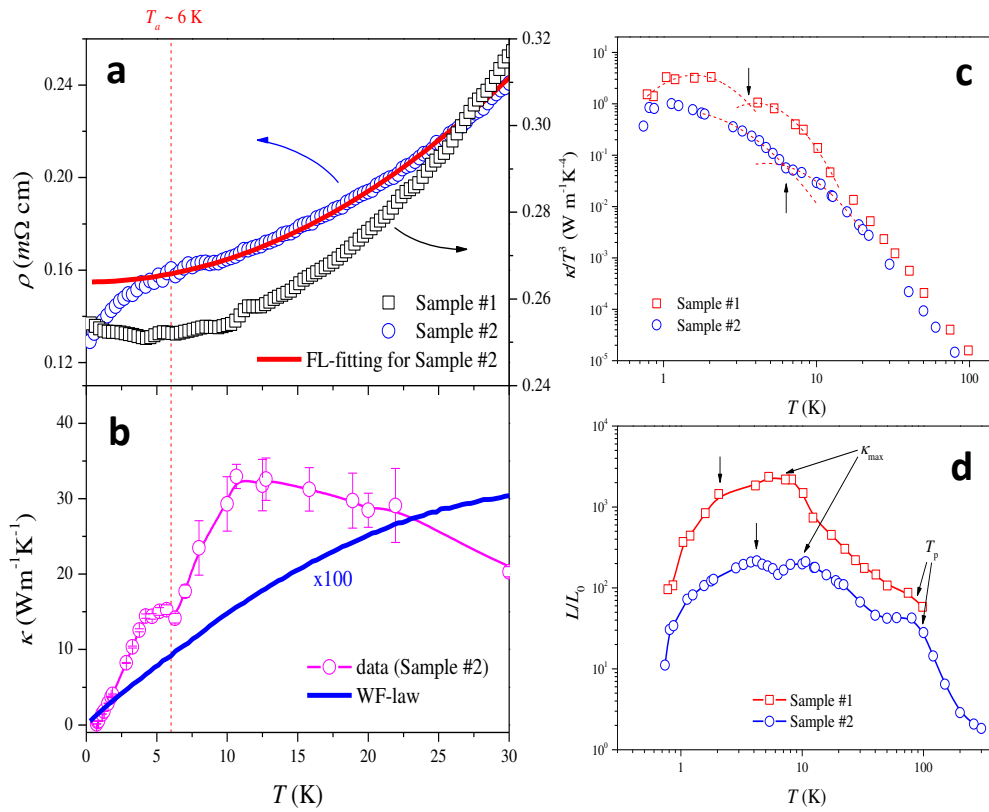


Figure 3. (a, b) Low- T electrical resistivity (Sample #1 and #2) and the thermal conductivity (Sample #2 only). The solid line (red) in (a) indicates a fitting result of the usual Fermi-liquid behavior. The Wiedemann-Franz law curve in (b) is plotted at 100x magnification for better comparison. (c) κ/T^3 and (d) Lorentz ratio (L/L_0) of two samples as a function of T . The vertical arrows in (c) and (d) indicate the kink and shoulder points, respectively. The dashed curves (red) in (c) are interpolated curves to show the kink-like anomaly.

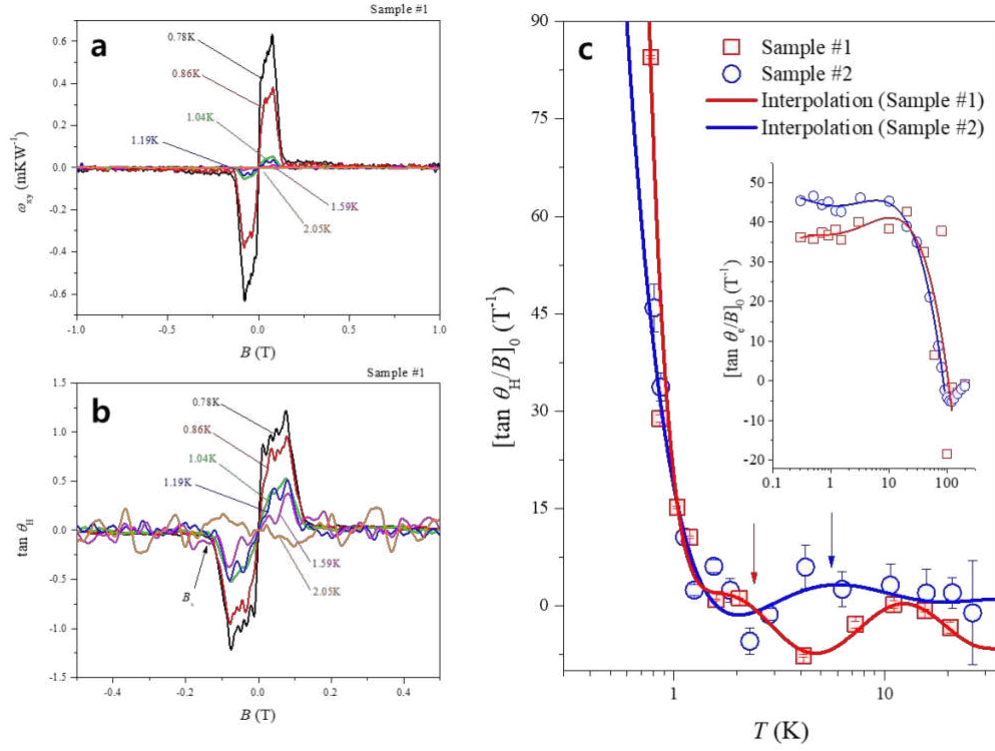


Figure 4. (a) Magnetic field dependence of thermal Hall resistivity ω_{xy} at different temperatures (Sample #1). (b) Tangential Hall angle ($\tan \theta_H = \frac{\kappa_{xy}}{\kappa_{xx}}$) in a magnetic field range of -0.5 to 0.5 T at various temperatures (Sample #1). (c) T -dependent slope of $\tan \theta_H$ of B in the zero magnetic field limit for two samples. Only the x-axis is presented with a logarithmic scale. In general, this value is proportional to the mean-free-path of the quasiparticles. The inset of (c) shows an initial slope of the electronic Hall angle identical to the thermal Hall angle. The vertical arrows denote the local maxima.

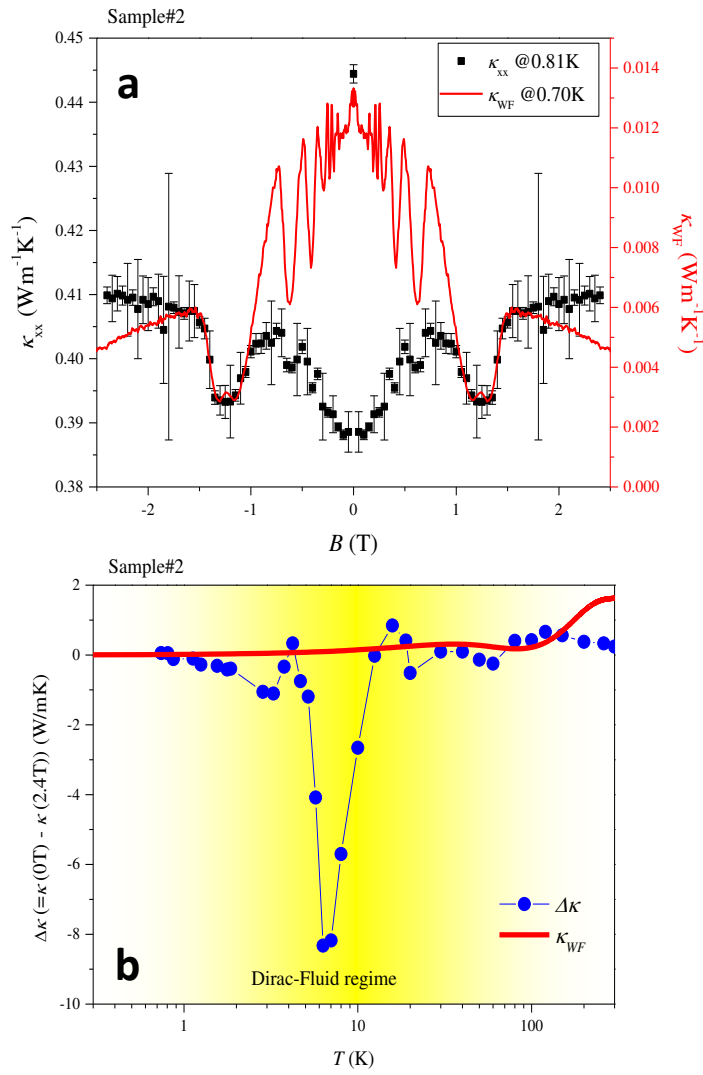


Figure 5. (a) Magnetic field dependent longitudinal total thermal conductivity κ_{xx} (closed squares) and purely electronic contributed thermal conductivity κ_{WF} (solid line). (b) The extracted Dirac particles contribution to the thermal conductivity in Sample #2 (closed circle). The κ_{WF} is calculated by the WF-law based on electrical resistivity data. $\Delta\kappa$ is strongly deviated in a hydrodynamic regime due to the Dirac-Fluid.

References

- 1 Phillipot, S. R. & McGaughey, A. J. H. Introduction to thermal transport. *Materials Today* **8** (6), 18-20 (2005).
- 2 Kaviany, M. *Principles of Heat Transfer*. (Wiley, 2002).
- 3 Ziman, J. M. *Electrons and Phonons: The Theory of Transport Phenomena in Solids*. (Oxford Univ. Press, 2001).
- 4 Dresselhaus, M. S. *et al.* New Directions for Low-Dimensional Thermoelectric Materials. *Adv. Mater.* **19**, 1043-1053 (2007).
- 5 Ackerman, C. C., Bertman, B., Fairbank, H. A. & Guyer, R. A. Second sound in solid helium. *Phys. Rev. Lett.* **16**, 789-791 (1966).
- 6 De Haas, W. J. & Biermasz, T. The thermal conductivity of KBr, KCl and SiO₂ at low temperatures. *Physica* **4**, 752-756 (1937).
- 7 Lee, S., Broido, D., Esfarjani, K. & Chen, G. Hydrodynamic phonon transport in suspended graphene. *Nat. Commun.* **6**, 6290 (2015).
- 8 Machida, Y., Matsumoto, N., Isono, T. & Behnia, K. Phonon hydrodynamics and ultrahigh-room-temperature thermal conductivity in thin graphite. *Science* **367**, 309-312 (2020).
- 9 Machida, Y. *et al.* Observation of Poiseuille flow of phonons in black phosphorus. *Sci. Adv.* **4**, eaat3374 (2018).
- 10 Huberman, S. *et al.* Observation of second sound in graphite at temperatures above 100 K. *Science* **364**, 375-379 (2019).
- 11 Crossno, J. *et al.* Observation of the Dirac fluid and the breakdown of the Wiedemann-Franz law in graphene. *Science* **351**, 1058-1061 (2016).
- 12 Martelli, V., Jimenez, J. L., Continentino, M., Baggio-Saitovitch, E. & Behnia, K. Thermal Transport and Phonon Hydrodynamics in Strontium Titanate. *Phys. Rev. Lett.* **120**, 125901 (2018).
- 13 Sussmann, J. A. & Thellung, A. Thermal Conductivity of Perfect Dielectric Crystals in the Absence of Umklapp Processes. *Proc. Phys. Soc.* **81**, 1122 (1963).
- 14 Guyer, R. A. & Krumhansl, J. A. Thermal Conductivity, Second Sound, and Phonon Hydrodynamic Phenomena in Nonmetallic Crystals. *Phys. Rev.* **148**, 778 (1966).
- 15 Cepellotti, A. *et al.* Phonon hydrodynamics in two-dimensional materials. *Nat. Commun.* **6**, 6400 (2015).
- 16 Li, X. & Lee, S. Crossover of ballistic, hydrodynamic, and diffusive phonon transport in suspended graphene. *Phys. Rev. B* **99**, 085202 (2019).
- 17 Martelli, V., Jimenez, J. L., Continentino, M., Baggio-Saitovitch, E. & Behnia, K. Thermal Transport and Phonon Hydrodynamics in Strontium Titanate. *Phys. Rev. Lett.* **120**, 125901 (2018).
- 18 Tang, F. *et al.* Three-dimensional quantum Hall effect and metal-insulator transition in ZrTe₅. *Nature* **569**, 537 (2019).
- 19 Weng, H., Dai, X. & Fang, Z. Transition-metal pentatelluride ZrTe₅ and HfTe₅: a paradigm for large-gap quantum spin Hall insulators. *Phys. Rev. X* **4**, 011002 (2014).
- 20 Li, Q. *et al.* Chiral magnetic effect in ZrTe₅. *Nature Physics* **12**, 550 (2016).
- 21 Fan, Z., Liang, Q.-F., Chen, Y. B., Yao, S.-H. & Zhou, J. Transition between strong and weak topological insulator in ZrTe₅ and HfTe₅. *Sci. Rep.* **7** (2017).
- 22 Mutch, J. *et al.* Evidence for a strain-tuned topological phase transition in ZrTe₅. *Sci. Adv.* **5** (2019).
- 23 Xu, B. *et al.* Temperature-Driven Topological Phase Transition and Intermediate Dirac Semimetal Phase in ZrTe₅. *Phys. Rev. Lett.* **121**, 187401 (2018).

- 24 Chi, H. *et al.* Lifshitz transition mediated electronic transport anomaly in bulk ZrTe₅. *New J. Phys.* **19**, 015005 (2017).
- 25 Zhou, Y. *et al.* Pressure-induced superconductivity in a three-dimensional topological material ZrTe₅. *Proc. Natl. Acad. Sci. USA* **113**, 2904 (2016).
- 26 Liang, T. *et al.* Anomalous Hall effect ZrTe₅. *Nat. Phys.* **14**, 451 (2018).
- 27 Fu, C. *et al.* Thermoelectric signatures of the electron-phonon fluid in PtSn₄. *arXiv*, 1802.09468 (2018).
- 28 Hirschberger, M., Krizan, J. W., Cava, R. J. & Ong, N. P. Large thermal Hall conductivity of neutral spin excitations in a frustrated quantum magnet. *Science* **348**, 106-109 (2015).
- 29 Kasahara, Y. *et al.* Anomalous quasiparticle transport and superclean superconducting state of CeCoIn₅. *Journal of Magnetism and Magnetic Materials* **310**, 569-571 (2007).
- 30 Wang, W. *et al.* Evidence for Layered Quantized Transport in Dirac Semimetal ZrTe₅. *Scientific Reports* **8**, 5125 (2018).
- 31 Yang, P. *et al.* Quantum Oscillations from Nontrivial States in Quasi-Two-Dimensional Dirac Semimetal ZrTe₅ Nanowires. *Scientific Reports* **9**, 3558 (2019).
- 32 Zheng, G. *et al.* Transport evidence for the three-dimensional Dirac semimetal phase in ZrTe₅. *Phys. Rev. B* **93**, 115414 (2016).
- 33 Zhang, W. *et al.* Observation of a thermoelectric Hall plateau in the extreme quantum limit. *Nat. Commun.* **11** (2020).

Supplementary Information for
Experimental observation of hydrodynamic-like behavior in 3D
topological semimetal ZrTe₅

Chang-woo Cho^{1,2}, Peipei Wang¹, Fangdong Tang¹, Sungkyun Park²,
Mingquan He³, Rolf Lortz⁴, Genda Gu⁵, and Liyuan Zhang^{1,+}

*¹Department of Physics, Southern University of Science and Technology, Shenzhen 518055,
China*

²Department of Physics, Pusan National University, Busan 46241, South Korea

*³Low Temperature Physics Lab, College of Physics & Center of Quantum Materials and
Devices, Chongqing University, Chongqing 401331, China*

*⁴Department of Physics, The Hong Kong University of Science and Technology, Clear Water
Bay, Kowloon, Hong Kong*

*⁵Condensed Matter Physics and Materials Science Department, Brookhaven National
Laboratory, Upton, NY 11973, USA*

⁺ corresponding author: zhangly@sustech.edu.cn

1. Thermal conductivity experimental set-up

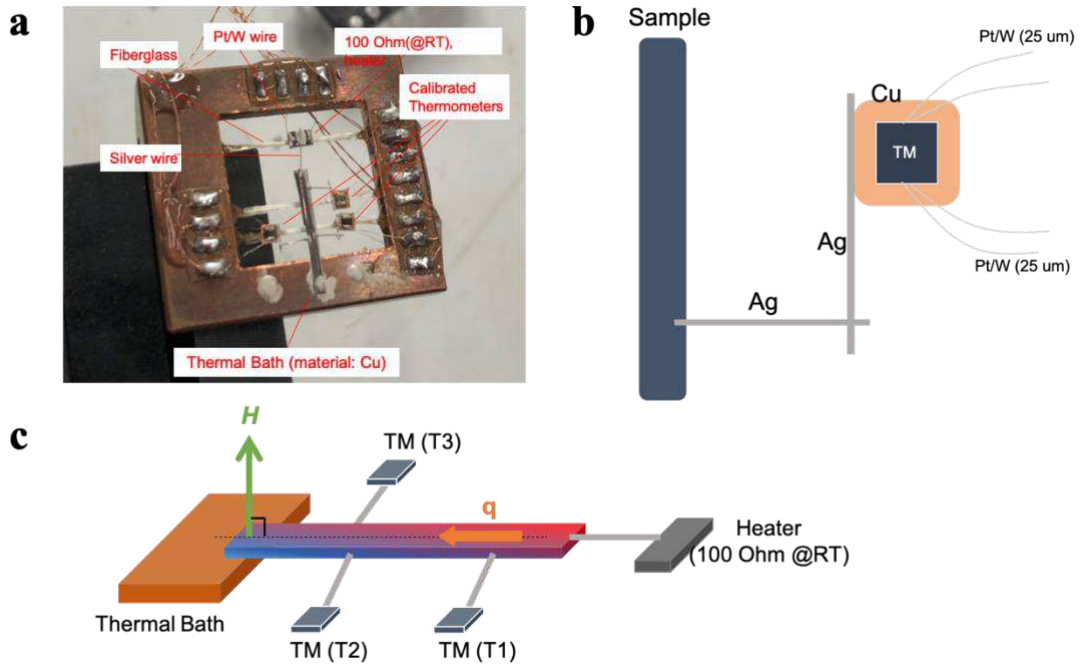


Figure S1. (a) Photograph of the thermal conductivity setup used in this study. (b) To minimize thermal leakage from the resistive heater to the thermal bath, we connected the sample to the heater and thermometers via 100 μm thick Ag-wires. While the connections for the electrical measurements are made by 25 μm thin Pt/W-wires (Pt/T is a good electrical conductor but a relatively poor thermal conductor). (c) Schematic diagram of our thermal conductivity experiment.

2. Two different method for the thermal conductivity measurement: thermometers vs thermocouples

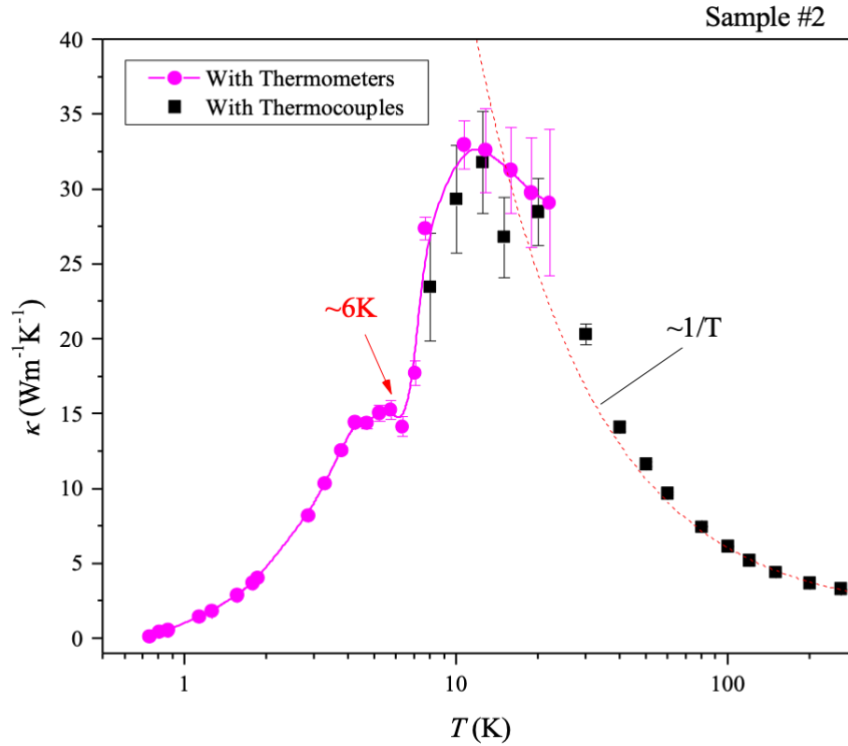


Figure S2. Thermal conductivity as a function of T for Sample #2. Thermometers were used because of their higher sensitivity at low temperatures due to their semiconducting nature with a large negative slope of their resistance (magenta). On the other hand, thermocouples are more sensitive at higher temperatures (black). In our experiments, we observe the overlapping T range from ~ 10 to ~ 20 K. The dashed curve (red) denotes the $1/T$ dependence curve.

3. Magnetic field dependence of electrical resistivity (Sample #2)

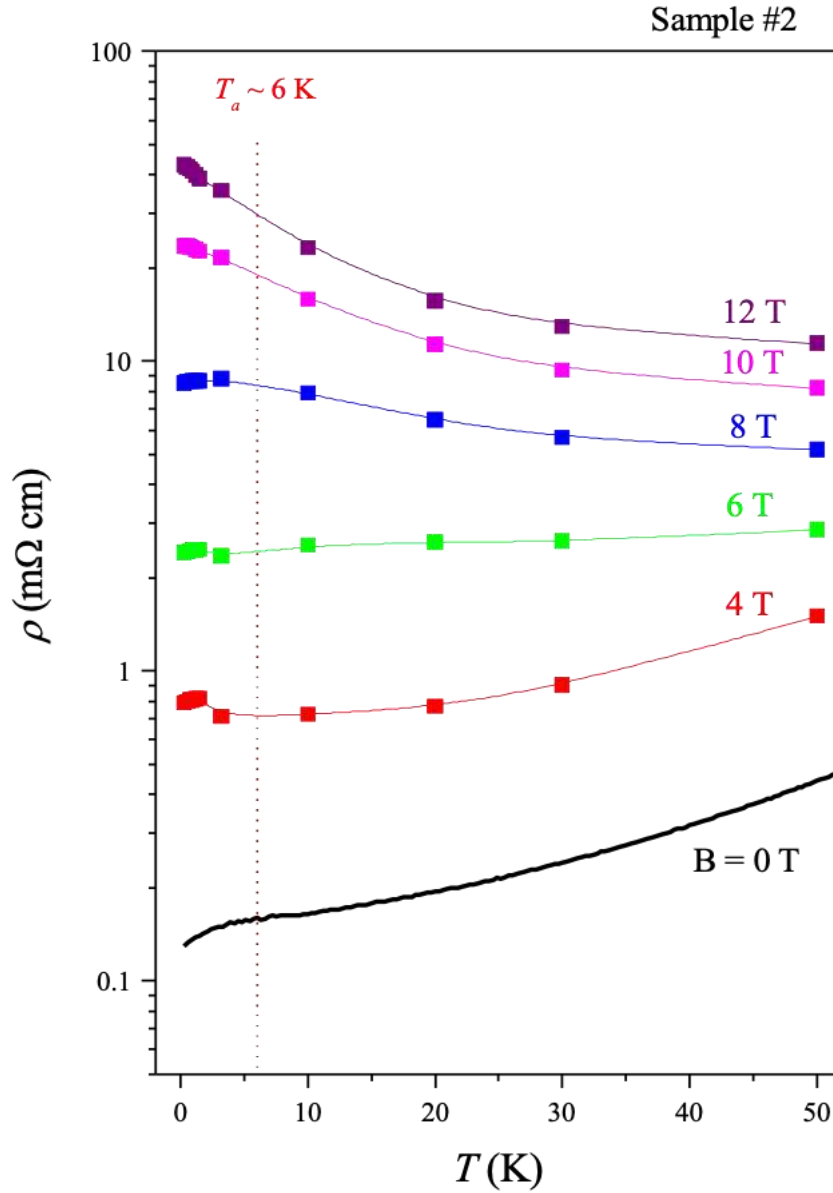


Figure S3. T dependence of electrical resistivity at various applied magnetic fields. Data at 0 T are measured during a T sweep, while field data are extracted from magneto-resistance (MR) data. An anomaly at T_a is seen at least up to 8 T, which greatly exceeds the reported critical field of pressure-induced superconductivity in ZrTe₅.

Figures

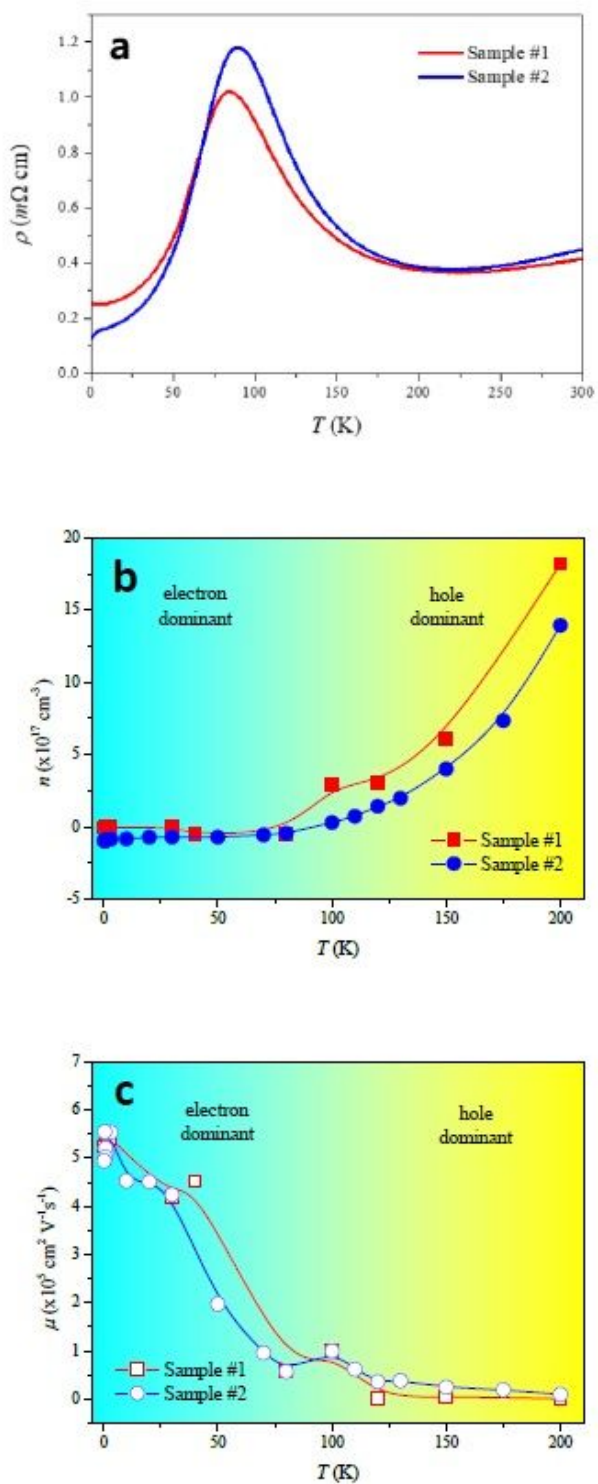


Figure 1

T-dependent electrical resistivity ρ (a), the dominant carrier density n (b), and their mobility μ (c) of ZrTe5 single crystals. To extract the n and μ , a two-band model was used for high T data (above 40 K), while the values at low T (below 40 K) were taken from the Hall measurement by the linear fitting method.

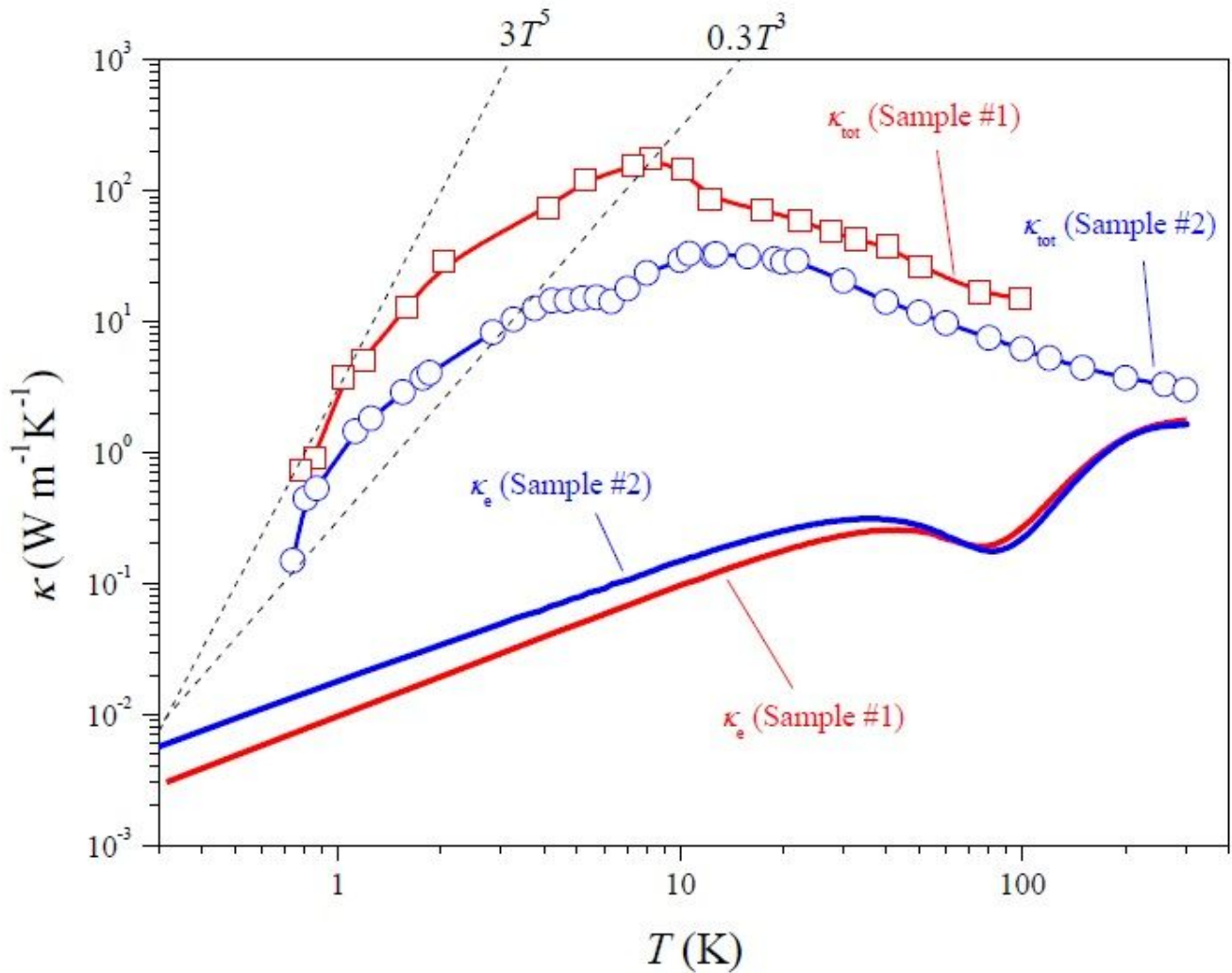


Figure 2

Thermal conductivity as a function of T in a log-log plot for two different ZrTe₅ samples. The open squares (Sample #1) and circles (Sample #2) represent the total thermal conductivity κ_{tot} , and the solid lines denote the charge carrier thermal conductivity κ_e , which is calculated according to the Wiedemann-Franz law ($\kappa_e = L \sigma T$, where the Lorenz number $L = 2.44 \times 10^{-8} \text{ W}\Omega^{-2}\text{K}^{-2}$). The two dashed lines proportional to T^3 and T^5 are added for comparison with the T evolution of κ_{tot} .

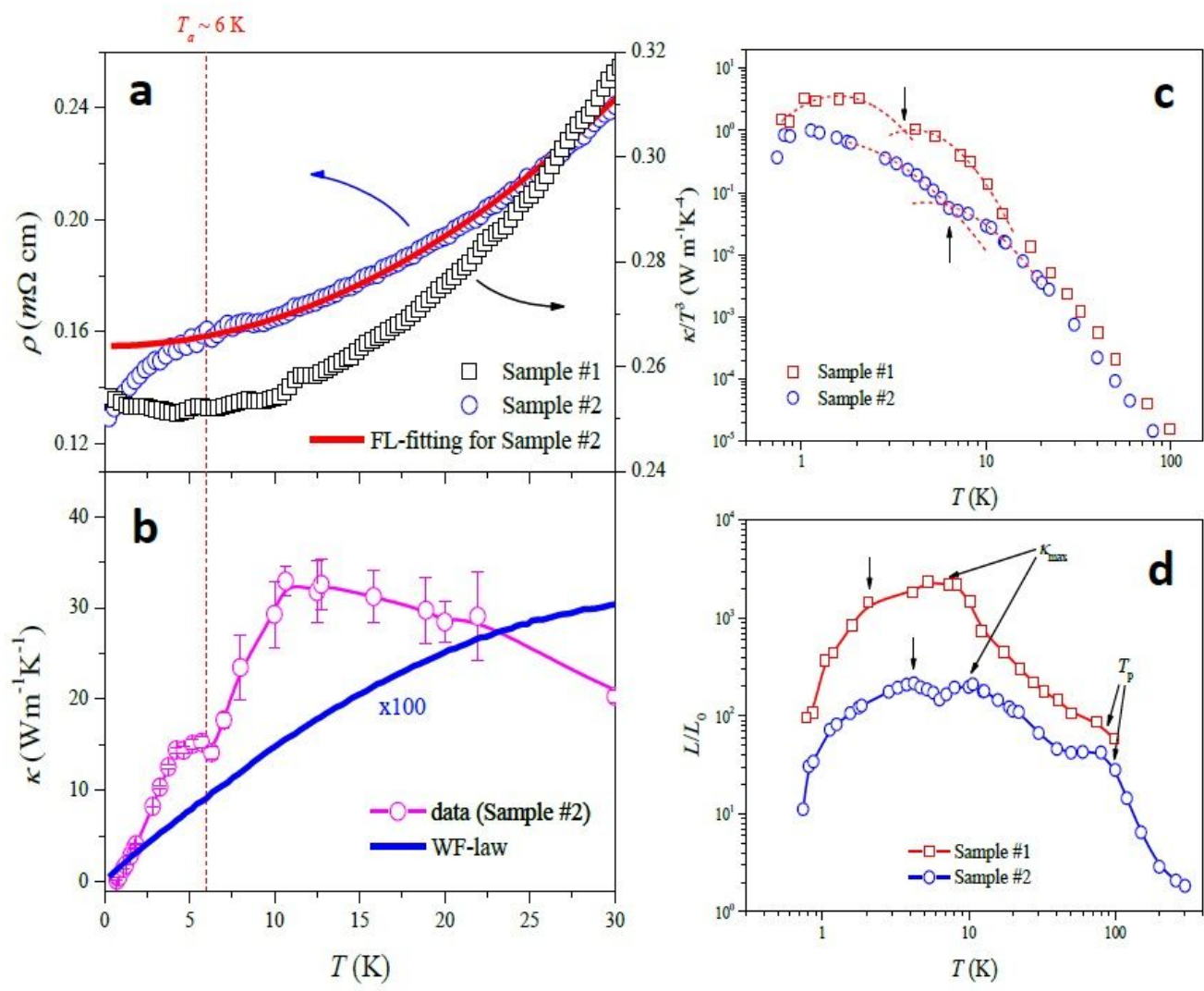


Figure 3

(a, b) Low-T electrical resistivity (Sample #1 and #2) and the thermal conductivity (Sample #2 only). The solid line (red) in (a) indicates a fitting result of the usual Fermi-liquid behavior. The Wiedemann-Franz law curve in (b) is plotted at 100x magnification for better comparison. (c) κ/T^3 and (d) Lorentz ratio (L/L_0) of two samples as a function of T . The vertical arrows in (c) and (d) indicate the kink and shoulder points, respectively. The dashed curves (red) in (c) are interpolated curves to show the kink-like anomaly.

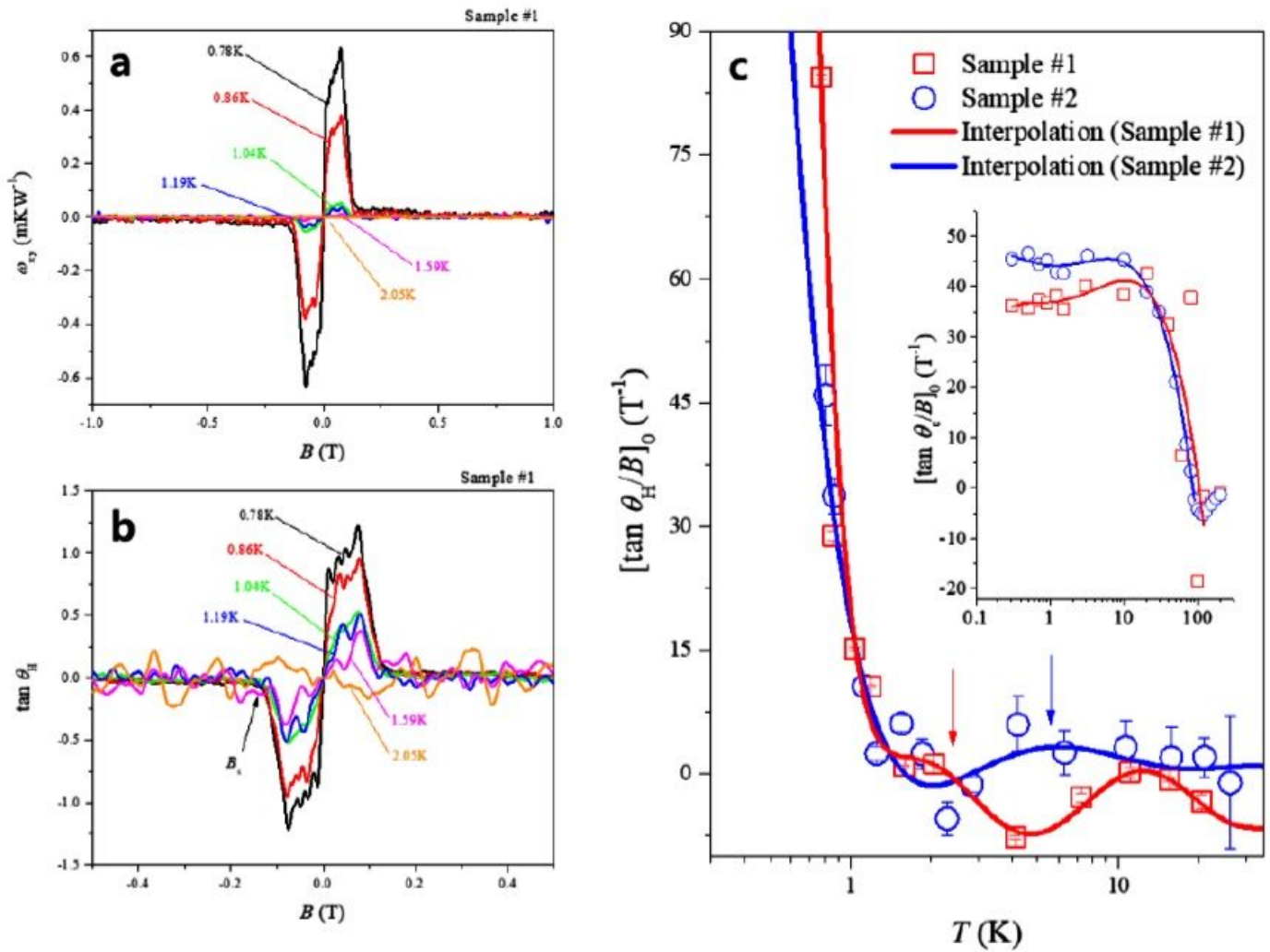


Figure 4

(a) Magnetic field dependence of thermal Hall resistivity ρ_{xy} at different temperatures (Sample #1). (b) Tangential Hall angle ($\tan \theta_H = \rho_{xy} / \rho_{xx}$) in a magnetic field range of -0.5 to 0.5 T at various temperatures (Sample #1). (c) T-dependent slope of $\tan \theta_H$ of B in the zero magnetic field limit for two samples. Only the x-axis is presented with a logarithmic scale. In general, this value is proportional to the mean-free-path of the quasiparticles. The inset of (c) shows an initial slope of the electronic Hall angle identical to the thermal Hall angle. The vertical arrows denote the local maxima.

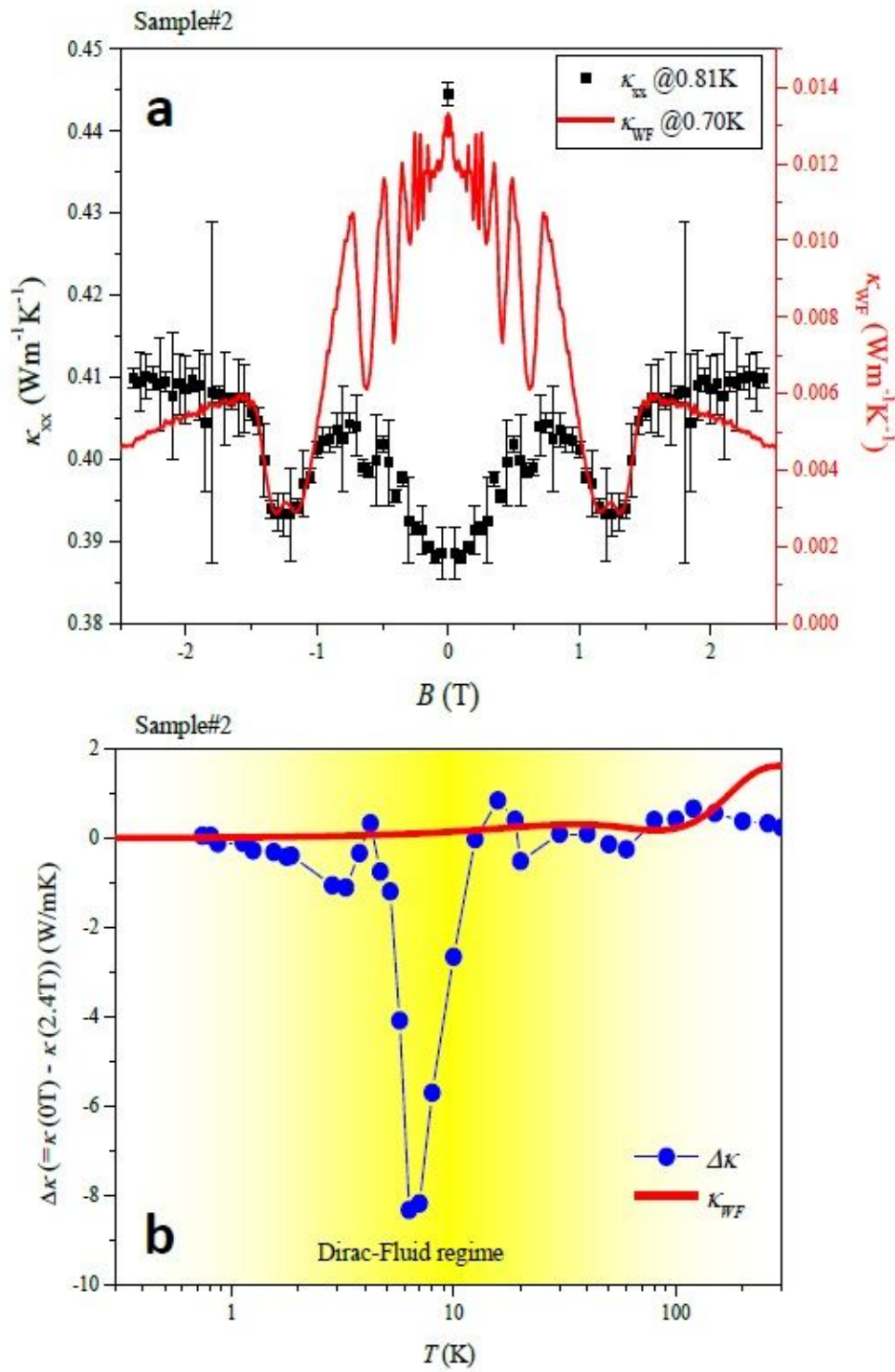


Figure 5

(a) Magnetic field dependent longitudinal total thermal conductivity κ_{xx} (closed squares) and purely electronic contributed thermal conductivity κ_{WF} (solid line). (b) The extracted Dirac particles contribution to the thermal conductivity in Sample #2 (closed circle). The κ_{WF} is calculated by the WF-law based on electrical resistivity data. $\Delta\kappa$ is strongly deviated in a hydrodynamic regime due to the Dirac-Fluid.